






RESEARCH ARTICLE | JULY 27 2023

# Turbulent dissipation in the boundary layer of precession-driven flow in a sphere

Sheng-An Shih (施勝安)  ; Santiago Andrés Triana ; Jérémy Requier ; Véronique Dehant 



AIP Advances 13, 075025 (2023)

<https://doi.org/10.1063/5.0146932>



CrossMark



## AIP Advances

### Special Topic: Machine Vision, Optical Sensing and Measurement

**Submit Today**



# Turbulent dissipation in the boundary layer of precession-driven flow in a sphere

Cite as: AIP Advances 13, 075025 (2023); doi: 10.1063/5.0146932

Submitted: 17 February 2023 • Accepted: 9 June 2023 •

Published Online: 27 July 2023



View Online



Export Citation



CrossMark

Sheng-An Shih (施勝安),<sup>1,2,a)</sup> Santiago Andrés Triana,<sup>2</sup> Jérémy Rekier,<sup>2</sup> and Véronique Dehant<sup>1,2</sup>

## AFFILIATIONS

<sup>1</sup> Université Catholique de Louvain, 1348 Ottignies-Louvain-la-Neuve, Belgium

<sup>2</sup> Royal Observatory of Belgium, 1180 Uccle, Belgium

<sup>a)</sup> Author to whom correspondence should be addressed: sheng-an.shih@oma.be

## ABSTRACT

The energy dissipation in a uniform vorticity flow, such as the flow in a precessing spheroid or the one associated with the earth's free core nutation, is mainly confined to the boundary layers. However, the thinness of the boundary layer renders it difficult to study the energy dissipation in the turbulent regime, either in laboratory experiments or through direct numerical simulations. Here, we use a local Cartesian model to study the energy dissipation in the boundary layer of a precessing sphere when the flow becomes turbulent, contrasting it with the laminar case. We compute the evolution of the boundary layer over time at individual co-latitudes based on direct numerical simulations using the computational fluid dynamics solver Nek5000. We then estimate the total global dissipation by summing up individual contributions. A comparison with known analytical results in the laminar case validates this approach. We briefly discuss the applications to the lunar and the earth's core cases.

© 2023 Author(s). All article content, except where otherwise noted, is licensed under a Creative Commons Attribution (CC BY) license (<http://creativecommons.org/licenses/by/4.0/>). <https://doi.org/10.1063/5.0146932>

## I. INTRODUCTION

Free Core Nutation (FCN) is a rotational normal mode of the earth. Since its frequency is close to forced nutation, the retrograde annual nutation, some properties of the FCN can be determined by measuring the resonant amplitude and the phase lag of the forced nutation [e.g., Herring *et al.* (1986)]. Inversions from the observed phase lag placed an upper bound for the fluid core kinematic viscosity of  $0.54 \text{ m}^2 \text{ s}^{-1}$  (Gwinn *et al.*, 1986), about six orders larger than the value inferred from studies of liquid metal [see the review of Lums and Aldridge (1991)]; a low viscosity of  $\nu = 10^{-6} \text{ m}^2 \text{ s}^{-1}$  is still favored by recent studies based on *ab initio* calculations [e.g., Pozzo *et al.* (2013) and Ichikawa and Tsuchiya (2015)]. Turbulence in the core's boundary layers can lead, in principle, to an enhanced eddy viscosity. However, Ohmic dissipation in the core and mantle is a more natural way to explain the observations [e.g., the studies by Buffett (1992), Mathews and Guo (2005), Deleplace and Cardin (2006), and Buffett and Christensen (2007)]. However, accounting for the observed phase lag requires either a strong magnetic field at the core-mantle boundary (CMB) or a highly conductive layer at the base of the mantle (Mathews *et al.*, 2002; Buffett *et al.*, 2002). Although the flow near the CMB associated with the FCN motion is

too weak to be turbulent, the flow associated with precession might be strong enough to be turbulent (Buffett, 2021; Triana *et al.*, 2021). Thus, it is important to properly quantify the turbulent contribution to the energy dissipation from precessional motion to obtain tighter bounds on the Ohmic dissipation.

Instabilities in the boundary layer of a precession-driven flow have been previously identified in numerical simulations (Lorenzani and Tilgner, 2001); however, the thinness of the boundary layer makes it difficult to study experimentally [see the review of Tilgner (2015)]. That same reason, combined with current computational constraints, precludes numerical studies from reaching regimes of parameters appropriate for planetary interiors where the Coriolis force plays a central role. This limitation is reflected in the smallness of the Ekman number  $E$ , representing the ratio of viscous to Coriolis forces and controlling the thickness  $L_v$  of the boundary layer (also known as the Ekman layer), which scales as  $L_v \propto E^{1/2}$ . We can define a local Reynolds number  $Re$  to quantify the condition for turbulence in the boundary layer as  $Re = UL_v/\nu$ , where  $\nu$  is the viscosity and  $U$  is the velocity. For the nominal value of the earth's precession-driven flow, the Reynolds number is about  $Re = 500$ , higher than the critical value of  $Re \sim 150$  for the onset of turbulence proposed by Sous *et al.* (2013). With a global spherical model, Cébron *et al.*

(2019) showed that the total viscous dissipation increases by a factor of 1.17 compared to the laminar solution when  $Re$  is around 230. Buffett (2021) restricted the modeling domain to the boundary layer and broke it into pieces according to the co-latitude  $\theta$ . Using a local Cartesian model, similar to ours, he studied two representative cases at  $\theta = 0$  and  $60^\circ$  and showed that the friction velocity  $u_*$ , a quantity proportional to the square root of the surface shear stress (see the definition below), increases by a factor of 1.2 at  $Re = 500$  compared to the laminar value. Buffett (2021) demonstrated a promising way to study the turbulent effects in the boundary layer from a local point of view. However, the connection to the global picture is still missing. Dissipation depends not only on the surface shear stress but also on the veering angle  $\beta$ , the angle between the stress and the fluid velocity on the boundary. In the present work, we numerically investigate the local flow at different co-latitudes and integrate the results to obtain global estimates of the possible turbulent energy dissipation.

Energy dissipation in the lunar core due to precession is a key parameter in understanding the possible dynamo action of the past (Stys and Dumberry, 2020; Zhang and Dumberry, 2021). The  $Re$  for the boundary layer flow is about  $10^4$ , much larger than earth's. Therefore, it has been believed that the boundary layer is turbulent [e.g., Yoder (1981)]. The model by Buffett (2021) is, in principle, not applicable to the moon not only because of the much higher Reynolds number but also because the flattening in their model must be much larger than the ratio of precession to rotation (i.e., the Poincaré number  $Po$ ). However, in the lunar case, the latter condition is not met as the CMB flattening of  $10^{-4}$  (Viswanathan et al., 2019) is smaller than the Poincaré number,  $Po = 4 \times 10^{-3}$ . In order to extend the result achieved by Buffett (2021), we investigate the problem by considering the case where the flattening is zero, i.e., a precessing fluid in a spherical cavity.

The scaling of quantities in the boundary layer can be used to estimate the dissipation at large  $Re$ . The theory for the scaling of  $u_*$  and  $\beta$  in the Ekman layer was proposed by Csanady (1967). It was later improved by Spalart (1989) by including higher order terms. Scaling has been studied via laboratory experiments (Caldwell et al., 1972; Sous et al., 2013) and numerical simulations (Coleman et al., 1990; Coleman, 1999; Shingai and Kawamura, 2004; Deusebio et al., 2014; and Braun et al., 2020). However, the Ekman layer in those studies is steady, i.e., it remains constant all the time, contrary to the one from precession-driven flow, which oscillates with diurnal frequency. The study of a Stokes boundary layer, an oscillating boundary layer but without Coriolis force, reveals complex behavior during the transition to turbulence: an instability growing in one oscillation cycle may eventually decay at intermediate  $Re$  (Ozdemir et al., 2014). Besides, analytical solutions show that the  $u_*$  associated with an oscillatory Ekman layer is smaller than that of a steady Ekman layer by a factor of  $2^{1/4}$  (Buffett, 2021). Therefore, we want to know if scaling is applicable to the oscillatory Ekman layer and establish the difference with those previous studies.

In Sec. II, we present the Navier–Stokes equation in the fluid frame using local Cartesian coordinates and compare it to the one used by Buffett (2021). Next, we outline the numerical implementation in Sec. III. Numerical solutions are presented in Sec. IV. Finally, the discussion and conclusions appear in Sec. V.

## II. PROBLEM FORMULATION

We consider a spherical cavity with radius  $R$  filled with an incompressible and viscous fluid, rotating with angular velocity  $\Omega_m$  and precessing with angular velocity  $\Omega_p$ . The angle between  $\Omega_m$  and  $\Omega_p$  is denoted as  $\alpha$ , the precession angle. In the case of weak precession ( $\Omega_p \ll \Omega_m$ ), the leading order solution for the flow in the cavity may be expressed as a solid body rotation  $\Omega_f$ , which represents the mean rotation vector of the fluid. Since the dominant forcing in the system is solely related to precession and the fluid viscosity  $\nu$ , the orientation of  $\Omega_f$  depends on their relative amplitudes. According to Busse's theory (Busse, 1968),  $\Omega_f$  can be determined, given the Poincare number  $Po = \Omega_p/\Omega_m$ , the Ekman number  $E = \nu/(\Omega_m R^2)$ , and the precession angle  $\alpha$ . We choose our reference frame as the one rotating with the fluid's mean angular velocity, and we refer to it as the fluid frame. In such a frame, the bulk of the fluid remains at rest, and the cavity rotates with  $\Delta\Omega = (\Omega_m - \Omega_f)$ . A boundary layer exists, the main focus of our study, with a nominal thickness  $L_v = \sqrt{\nu/\Omega_f}$ .

In the fluid frame, we define two Cartesian coordinate systems: one global ( $\hat{X}, \hat{Y}, \hat{Z}$ ) and one local ( $\hat{x}, \hat{y}, \hat{z}$ ) (Fig. 1). For the global coordinate system,  $\hat{Z}$  is aligned with  $\Omega_f$ , and the coordinate system co-rotates with the fluid. For the local coordinate system, the  $x$ -axis is eastward, the  $y$ -axis is northward, and the  $z$ -axis is in the radial outward direction. The fluid domain extends from  $z = 0$  toward the negative  $z$ -axis. In the fluid frame, the flow velocity  $\mathbf{u}$  satisfies the following Navier–Stokes equation:

$$\frac{\partial \mathbf{u}}{\partial t} + \mathbf{u} \cdot \nabla \mathbf{u} + 2(\Omega_f + \Omega_p) \times \mathbf{u} = -\frac{\nabla P}{\rho} + \nu \nabla^2 \mathbf{u} + \mathbf{r}' \times (\Omega_p \times \Omega_f), \tag{1}$$

where  $P$  is the reduced pressure including the centrifugal force and  $\mathbf{r}'$  is the position vector referring to any point inside the cavity. The last term,  $\mathbf{r}' \times (\Omega_p \times \Omega_f)$ , is known as the Poincaré term [coined by Malkus (1968)] or the Euler term, which is associated with the fictitious force appearing in such a non-uniformly rotating reference frame. Since the flow is mainly confined to the viscous boundary layer, we take  $L_v$  as the length scale to analyze Eq. (1). We further assume that  $L_v$  is much smaller than the cavity radius  $R$ , so the cavity curvature is neglected in the local model. Together with the differential velocity  $U = R|\Delta\Omega|$  as the velocity scale, Eq. (1) can be written in dimensionless form as

$$\begin{aligned} \frac{\partial \mathbf{u}^*}{\partial t^*} + \mathbf{u}^* \cdot \nabla^* \mathbf{u}^* + \frac{2}{Re} \left[ \hat{\mathbf{k}}_f + Po \left( \frac{\Omega_m}{\Omega_f} \right) \hat{\mathbf{k}}_p \right] \times \mathbf{u}^* \\ = -\nabla^* P^* + \frac{1}{Re} \nabla^{*2} \mathbf{u}^* + \left( \frac{L_v}{R} \right) \left( \frac{\Omega_m}{\Delta\Omega} \right)^2 Po \left( \frac{\Omega_f}{\Omega_m} \right) \\ \times \left[ \left( \frac{L_v}{R} \right) \mathbf{r}^* + \hat{\mathbf{R}} \right] (\hat{\mathbf{k}}_p \times \hat{\mathbf{k}}_f), \end{aligned} \tag{2}$$

where  $Re = UL_v/\nu$  is the Reynolds number and  $\hat{\mathbf{R}} = \mathbf{R}/R$  is a unit vector. A superscript (\*) denotes dimensionless variables (the variable  $\mathbf{u}^*$  is not to be confused with the friction velocity  $u_*$  introduced later). In the local coordinate system, the vector  $\hat{\mathbf{k}}_f$  is given by  $\cos \theta \hat{\mathbf{z}} + \sin \theta \hat{\mathbf{y}}$ , where  $\theta$  is the co-latitude.

Before moving on to the boundary conditions, we find it necessary to specify the orientations of  $\Omega_m$  and  $\Omega_f$  in a coordinate system defined in the precessing frame, which rotates with  $\Omega_p$ . In

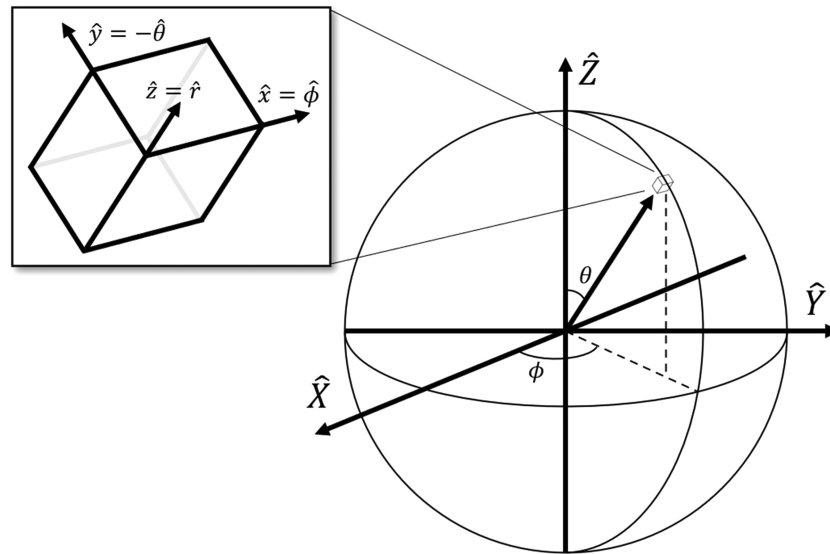


**FIG. 1.** Sketch of a spherical cavity with a local box. Two coordinate systems are shown: global  $(\hat{X}, \hat{Y}, \hat{Z})$  and local  $(\hat{x}, \hat{y}, \hat{z})$ . The two vectors  $\hat{x}$  and  $\hat{y}$  denote the unit vectors along the directions of longitude  $\phi$  and (negative) co-latitude  $\theta$ , respectively.

the precessing frame, both vectors are stationary based on the theory proposed by Busse (1968). The coordinate system, denoted as  $(\hat{X}_p, \hat{Y}_p, \hat{Z}_p)$ , is defined such that it coincides with  $(\hat{X}, \hat{Y}, \hat{Z})$  at  $t = 0$ ; otherwise, the latter is rotating with  $\Omega_f$  in the precessing frame. Moreover,  $\Omega_m$  is tilted toward negative  $\hat{X}_p$ , forming an angle  $\theta_f$  relative to  $\Omega_f$  (see below for the definition of  $\theta_f$ ). Under the no spin-up condition (i.e.,  $\Omega_f = \Omega_m \sin \theta_f$ ), the differential rotation vector will be lying on the equatorial plane:  $\Delta\Omega = -\Delta\Omega\hat{X}_p$ . The coordinate is then transformed to  $(\hat{X}, \hat{Y}, \hat{Z})$  in the fluid frame and further to  $(\hat{x}, \hat{y}, \hat{z})$  for the computation of boundary velocity, which is  $\Delta\Omega \times \mathbf{R}$ . Explicit expressions of the transformations are given in Appendix A. In the local coordinate system, the boundary condition at the lower end ( $z^* \rightarrow -\infty$ ) is  $\mathbf{u}^* = 0$  (i.e., the bulk of the fluid sufficiently away from the boundary is at rest). Note that, in the numerical implementation discussed below, the lower end is set at  $z^* = -30$ . On the fluid surface ( $z^* = 0$ , corresponding to the CMB),

$$u_x^* = \cos \theta \cos (\Omega_f t + \phi), \quad (3a)$$

$$u_y^* = -\sin (\Omega_f t + \phi), \quad (3b)$$

$$u_z^* = 0, \quad (3c)$$

where  $\phi$  is the longitude. Thanks to the azimuthal  $m = 1$  symmetry of the flow, it is anticipated that the local flow field at a given  $\phi_0$  is equivalent to the flow at the prime meridian ( $\phi = 0$ ) with a lag time  $\phi_0/\Omega_f$ . For the numerical implementation, we set  $\phi = 0$ , and then the azimuthal dependence is retrieved directly from  $\Omega_f t$  for post-processing analysis, that is, a time-average can be treated as an azimuthal average.

To determine  $\Omega_f$ , we use the reduced model developed by Cébron *et al.* (2019) [i.e., their Eqs. (5)–(7)]. Their solutions are

obtained in the precessing frame where a Cartesian coordinate system  $(\hat{X}'_p, \hat{Y}'_p, \hat{Z}'_p)$  is defined such that the  $\hat{Z}'_p$ -axis and  $\Omega_m$  are aligned. The spherical coordinates of  $\Omega_f$  are denoted as the co-latitude  $\theta_f$  and the longitude  $\phi_f$ . The coordinates are transformed to the local system by three steps: (1) rotation of the coordinate system to align the  $\hat{Z}'_p$ -axis with  $\Omega_f$ , (2) transformation from the precessing frame to the fluid frame, and (3) transformation from the global system to the local system. Details about the transformation are given in Appendix A. So far, we are ready to solve Eq. (2) numerically.

We use the lunar parameters listed in Table I as an end-member case to estimate the amplitude of the Poincaré term, where  $|\hat{k}_p \times \hat{k}_f| = \sin \gamma$ , and find that the amplitude is  $3 \times 10^{-10}$ . The ratio of the amplitudes of the Poincaré term to the viscous term is  $4 \times 10^{-6}$ , which is the value obtained in the turbulent regime where  $Re = 1.67 \times 10^4$ . In the laminar regime, say  $Re = 5$ , we find the ratio is  $7 \times 10^{-3}$ , thus allowing us to drop the Poincaré term in the  $Re$  range discussed in the present study. Second, we consider the magnitude of  $(\Omega_m/\Omega_f)$ , which is equal to  $\cos^{-1} \theta_f$  under the no spin-up condition. Given  $\theta_f = 1.543^\circ$  at  $Re = 1.67 \times 10^4$ , the magnitude is very close to unity with a difference of 0.04%. With lower  $Re$  (high  $\nu$ ), the angle  $\theta_f$  will be even smaller, thus making  $(\Omega_f/\Omega_m)$  closer to unity. Third, the condition of weak precession ( $Po \ll 1$ ) allows us to drop the precession vector in the Coriolis term. With these approximations, we arrive to the reduced form of Eq. (2),

$$\frac{\partial \mathbf{u}^*}{\partial t^*} + \mathbf{u}^* \cdot \nabla^* \mathbf{u}^* + \frac{1}{Re} (2\hat{k}_f \times \mathbf{u}^*) = -\nabla^* P^* + \frac{1}{Re} \nabla^{*2} \mathbf{u}^*. \quad (4)$$

For comparison, we numerically solve both Eqs. (2) and (4) at  $Re = 500$  and find no significant difference between the two solutions (see Fig. S1 in the supplementary material). In other words, neglecting the precessional terms makes no difference in our case. In the following, all the discussions will be based on Eq. (4). We

**TABLE I.** Lunar parameters used in this study.  $R$  is the radius of the lunar core-mantle boundary (Viswanathan *et al.*, 2019).  $\alpha$  is the angle between the symmetry axis and the ecliptic normal. We use Eqs. (5)–(7) of the study by Cébron *et al.* (2019) to compute  $\Omega_f$ ; the orientation  $(\theta_f, \phi_f)$  is given by the coordinate system  $(\hat{X}_p, \hat{Y}_p, \hat{Z}_p)$  whose  $\hat{Z}_p$  is aligned with  $\Omega_m$  (see Appendix A). The angle between  $\Omega_f$  and  $\Omega_p$  is denoted by  $\gamma$ .

Parameter	Definition	Units	Value
$\nu$		$\text{m}^2 \text{s}^{-1}$	$10^{-6}$
$\Omega_m$		$\text{rad s}^{-1}$	$2.66 \times 10^{-6}$
$\Omega_f$	$\Omega_m \cos \theta_f$	$\text{rad s}^{-1}$	$2.659 \times 10^{-6}$
$\Omega_p$		$\text{rad s}^{-1}$	$1.07 \times 10^{-8}$
$R$		km	380
$L_\nu$	$\sqrt{\nu/\Omega_f}$	m	0.61
$\alpha$		deg	1.543
$\theta_f$		deg	1.543
$\phi_f$		deg	0.060
$\gamma$		deg	0.002
$U$	$R\Omega_m \sin \theta_f$	$\text{m s}^{-1}$	$2.72 \times 10^{-2}$
$Po$	$\Omega_p/\Omega_m$		$4 \times 10^{-3}$
$E$	$\nu/(R^2\Omega_m)$		$3 \times 10^{-12}$
$Re$	$UL_\nu/\nu$		$1.67 \times 10^4$

note that Eq. (4) is generally identical to the one derived for a precessing spheroidal cavity [see the Appendix of the study by Buffett (2021)], even though the reasons to drop the Poincaré term are different. In a precessing spheroid, the Poincaré term is balanced by the terms associated with the flattening. Nevertheless, both formulations make the governing equation resemble a simple rotating fluid. The appearance of Eq. (4) may seem counter-intuitive indeed, but it is important to remember the initial assumption that the container is precessing and that the flow is mostly a uniform vorticity flow. The local model aims to examine the flow in a small rectangular box near the boundary. Precession comes into play when we determine  $\Omega_f$ . The only difference to the study by Buffett (2021) lies in the selection of the rotation vector, where we employ  $\Omega_f$  in contrast to  $\Omega_m$  used by Buffett. Considering the aforementioned assumption, that is,  $\Omega_f/\Omega_m \approx 1$ , the discrepancy between the two vectors becomes negligible. Nevertheless, we think that adopting  $\Omega_f$  is more appropriate and self-consistent as the local model requires the bulk fluid to be at rest, a condition that may not hold when employing  $\Omega_m$  in the mantle frame. In Appendix B, we derive the analytical solution in the laminar regime where  $Re$  is small and the non-linear term can be neglected, which matches the numerical result, as expected.

Next, we compute the dissipation in the boundary layer. In the local system, the input (output) power from the surface shear stress  $\boldsymbol{\tau}$  is equal to the increase (decrease) of internal and kinetic energies [see, e.g., Sec. 16 in the study by Landau and Lifschitz (2013)],

$$S(\mathbf{u} \cdot \boldsymbol{\tau})_{z=0} = \dot{E}_{\text{int}} + \dot{E}_{\text{kin}}, \quad (5)$$

where  $S$  is the surface area. The increase in internal energy is further linked to the energy dissipated in the system. Therefore, for an equilibrium system where the change in kinetic energy reaches zero, the viscous power can be used to infer the dissipation. Suppose

that the area  $S$  corresponds to a small patch on the cavity surface  $dS = \sin \theta R^2 d\theta d\phi$ , we compute the total dissipation via  $\mathcal{D}_\nu = -\int (\boldsymbol{\tau} \cdot \mathbf{u}) dS$ . The local viscous power per unit area is defined as  $\mathcal{P}^{\text{visc}} = \boldsymbol{\tau} \cdot \mathbf{u}$  for later use. We can integrate the laminar analytical solutions to obtain the global laminar dissipation as [e.g., in the study by Cébron *et al.* (2019)]

$$\mathcal{D}_\nu^{\text{lam}} = -2.62 I \Delta \Omega^2 \sqrt{\nu \Omega} / R, \quad (6)$$

where  $I = (8\pi/15)\rho R^5$  is the moment of inertia of the fluid. This result is consistent with the torque approach, which is given in Appendix B. A script for the computation is included in the supplementary material.

In the turbulent regime, the surface shear stress no longer follows the analytical solution, so we prescribe the turbulent stress as  $k\rho|\mathbf{u}|\mathbf{u}$  [e.g., in the study by Williams *et al.* (2001)], where  $k$  is a dimensionless parameter that depends on the viscosity. The total turbulent dissipation  $-(45\pi/32)kI\Delta\Omega^3$  is obtained by integrating the negative viscous power over the spherical surface. Since dissipation is independent of the orientation of  $\Delta\Omega$ , one can take  $\Delta\Omega = \Delta\Omega\hat{\mathbf{Z}}$  to simplify the computation, as performed by Yoder (1981). For an arbitrary orientation, we obtain the same coefficient,  $-(45\pi/32)$ , by approximating the integral as a Riemann sum. Note that the stress prescription assumes that the stress is aligned with the velocity, which is not true for most cases (see Fig. S10 for the veering angle at different values of  $\theta$ ), so the turbulent torque derived from this definition should thus be treated with extra care. In order to determine the parameter  $k$ , we adopt the approach by Cébron *et al.* (2019) and require  $\mathcal{P}^{\text{visc}}$ , computed from turbulent and laminar stresses (B17) and (B18), to match  $\theta = 0$ ; it gives  $k = (u_*/U)^2 \cos \beta$ , where  $u_* = \sqrt{|\boldsymbol{\tau}|/\rho}$  is the friction velocity and  $\beta$  is the veering angle, the angle between the surface shear stress and the fluid velocity on the boundary. We notice that, when we substitute the laminar solutions  $u_* = \sqrt{\nu U/L_\nu}$  and  $\beta = 45^\circ$  into  $k$  and compute the total turbulent dissipation, the obtained dissipation disagrees with the laminar expectation given in Eq. (6). To reconcile the inconsistency, we define the turbulent dissipation as

$$\mathcal{D}_\nu^{\text{turb}} = -2.62 \sqrt{2} k I \Delta \Omega^3, \quad (7)$$

In principle, one can match  $\mathcal{P}^{\text{visc}}$  at any  $\theta$ . We choose  $\theta = 0$  because the asymptotic similarity theory is used to estimate the friction velocity and veering angle at this special case, where the presence of a logarithmic layer supports the use of the theory. The purpose of this modification is to provide a way to compute  $k$  and relate it to the total dissipation, which can be compared to our numerical results.

### III. NUMERICAL IMPLEMENTATION

We use the spectral element code Nek5000 (Fischer *et al.*, 2007) to solve Eq. (4) for an incompressible fluid in a Cartesian box. The domain is divided into  $\mathcal{E}$  elements, where solutions are represented by  $N$ -th order Lagrange interpolation polynomials (see Fig. 2). The typical resolution in the present study is  $\mathcal{E} = 768$  and  $N = 9$ . The temporal discretization is based on a third-order backward-difference scheme for implicit terms and on an extrapolation scheme for explicit terms. We use dealiasing following the 3/2 rule.

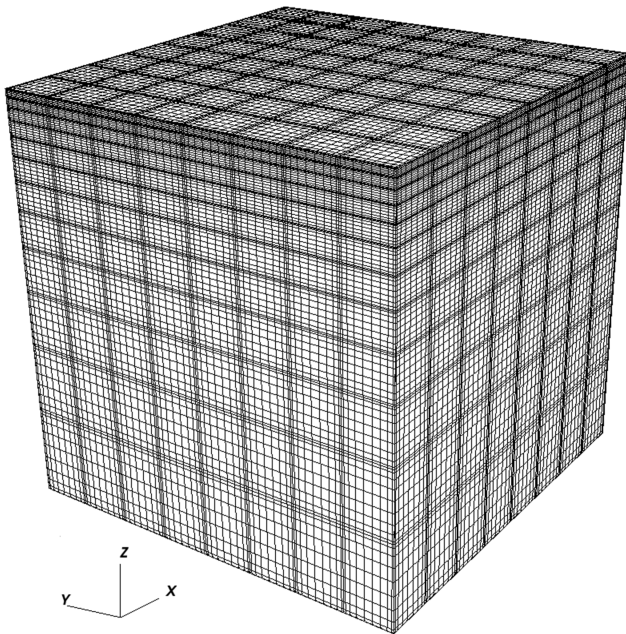


**FIG. 2.** Box model with Cartesian coordinates. The typical resolution is  $\mathcal{E} = 768$  and  $N = 9$ . The dimension of the box is  $30 \times 30 \times 30$  in the unit of  $L_v$ . The element density is higher near the top boundary to resolve the boundary flow.

The domain is extended downward from  $z = 0$ . The non-dimensional size is  $30 \times 30 \times 30$ . The top boundary is a wall (representing the CMB), where the velocity is specified to mimic the precessing container (mantle), as seen from the fluid frame [see Eq. (3)]. The four lateral boundaries are periodic. The bottom boundary is stress-free (i.e., no tangential stress), and the normal velocity is zero. We have performed a height test to make sure that the domain height of  $30L_v$  is large enough to accommodate the boundary layer flow (see Fig. S2 in the supplementary material). To resolve the boundary layer flow, we use a higher element density near the top boundary. We will explore the parameter space:  $Re = [5, 500]$  and  $\theta = [0, 90^\circ]$ . Simulations for  $Re = 700$  are added to extend the  $Re$  range. We also simulate the case with  $Re = 600$  at  $\theta = 0$ . The range of  $Re$  covers both the laminar and turbulent regimes of the oscillatory Ekman layer.

The simulation always starts from the fluid at rest, where a random perturbation in velocity with root-mean-square amplitude of about  $10^{-2}$  is imposed. In most cases, the flow will go through a transient state for a certain period and reach a *statistically steady state* (we shall refer to it as a steady state for the sake of brevity in the following sections), which means time-averaged quantities over the oscillation period(s) remain constant. The mean values presented below are obtained by taking time averages over oscillation periods. Due to the homogeneity on  $x$ - and  $y$ -directions, all the values are also averaged on the horizontal plane. The unit of time  $t_\oplus$  presented below is  $2\pi/\Omega_f$ , indicating the period of the oscillating boundary. In what follows, the superscript (+) denotes the quantities non-dimensionalized by the viscous wall scales, velocity  $u_*$ , and length  $v/u_*$ . The notation is chosen to describe the flow near the boundary.

## IV. RESULTS

We present now our numerical results, comparing them with analytical solutions, highlighting the difference between laminar and turbulent regimes. Then we use the numerical results in the turbulent regime together with the asymptotic theory to construct a turbulence model for the energy dissipation. Finally, we compute the total dissipation based on the local model and calibrate the turbulence model accordingly.

### A. Friction velocity and kinetic energy

The friction velocity  $u_*$  is a quantity commonly used to monitor the amplitude of surface shear stress  $|\tau|$ :  $u_* = \sqrt{|\tau|/\rho}$  [e.g., in the study by Tennekes *et al.* (1972)]. At  $\theta = 0$ , Eqs. (B19) and (B20) give the laminar solution  $u_*^{\text{lam}} = Re^{-1/2}U$ , which serves as the benchmark for low Reynolds number cases. Figure 3 shows the ratio  $u_*/u_*^{\text{lam}}$  as a function of time at  $\theta = 0$  for different values of  $Re$ . We see that the friction velocity deviates from its laminar solution when  $Re \geq 300$  and the deviation is larger for higher  $Re$ . Concerning the case of  $Re = 300$ , it appears that the deviation from the laminar solution by about 10% can be attributed to turbulence, as supported by the presence of a logarithmic region presented later in this study. We observe that the transient period happens before  $t_\oplus = 3$  (before  $t_\oplus = 1$  for  $Re = 400$  and higher) and the friction velocity reaches a steady value. The result is consistent with the one from the study by Buffett (2021), where the solution at  $Re = 500$  is about 20% larger than the laminar value after the onset of turbulence. To obtain the mean value, we take a time average over the interval  $1 \leq t_\oplus \leq 5$ , except for  $Re = 300$  where we use the  $3 < t_\oplus < 5$  interval (see Table II).

Figure 4 shows the total kinetic energy,  $E_{\text{kin}}$ , for  $Re = 500$  at different values of  $\theta$ . We observe that the total kinetic energies reach a steady state for *most* cases. It implies that the time-averaged change in the kinetic energy is zero,  $\langle \dot{E}_{\text{kin}} \rangle = 0$ , and the system is in equilibrium state. According to Eq. (5), we can use the viscous power to approximate the dissipation. Although we can compute the

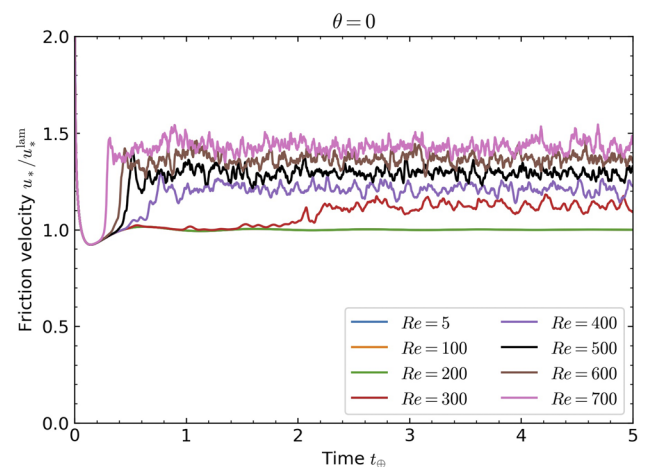


**FIG. 3.** Friction velocity ratio  $u_*/u_*^{\text{lam}}$  as a function of time with different values of  $Re$  at  $\theta = 0$ . The means deviate appreciably from unity when  $Re \geq 300$  and almost reach 1.3 when  $Re = 500$ . The  $Re = 5, 100, 200$  curves overlap nearly completely.

**TABLE II.** Main results of the present study. Time-averaged values are obtained from the range  $1 \leq t_{\oplus} \leq 5$ , except for the case  $Re = 300$  where the range used is  $3 \leq t_{\oplus} \leq 5$ . The values of the friction velocity and the veering angle are obtained from the cases with  $\theta = 0$ .

$Re$	$\langle u_* \rangle / u_*^{\text{lam}}$	$\langle u_* \rangle / U$	$\langle \beta \rangle$ (deg)	$\langle \mathcal{D}_v \rangle / \mathcal{D}_v^{\text{lam}}$
5	$1.00 \pm 0.00$	$0.447\,192 \pm 0.000\,419$	$45.002\,058 \pm 0.095\,827$	0.96
100	$1.00 \pm 0.00$	$0.099\,973 \pm 0.000\,224$	$45.010\,85 \pm 0.229\,41$	0.96
200	$1.00 \pm 0.00$	$0.070\,693 \pm 0.000\,158$	$45.010\,364 \pm 0.229\,03$	0.97
300	$1.13 \pm 0.02$	$0.064\,989 \pm 0.001\,234$	$29.350\,199 \pm 1.461\,621$	1.34
400	$1.21 \pm 0.02$	$0.060\,584 \pm 0.001\,197$	$25.635\,712 \pm 1.273\,489$	1.61
500	$1.29 \pm 0.03$	$0.057\,866 \pm 0.001\,131$	$22.978\,039 \pm 1.135\,976$	1.86
600	$1.37 \pm 0.03$	$0.055\,831 \pm 0.001\,122$	$21.037\,396 \pm 1.317\,849$	...
700	$1.43 \pm 0.03$	$0.054\,069 \pm 0.001\,123$	$20.081\,535 \pm 1.411\,917$	2.42

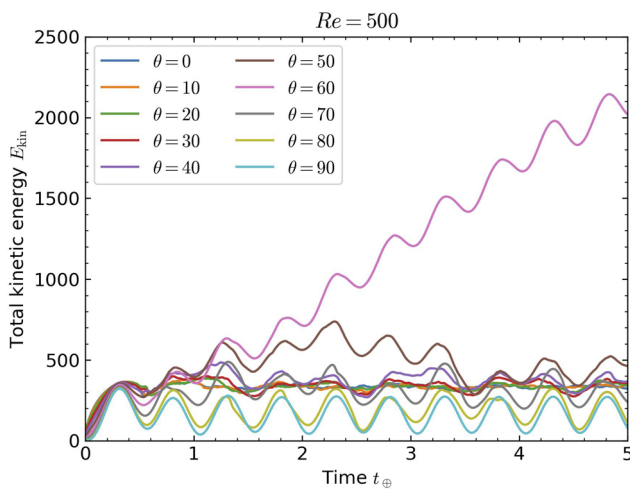


**FIG. 4.** Total kinetic energy  $E_{\text{kin}}$  with different values of  $\theta$  at  $Re = 500$ . Most cases reach steady state within  $t_{\oplus} = 5$ , while a long-period modulation is observed for  $\theta = 50^\circ$  and an indefinite increase is observed for  $\theta = 60^\circ$ .

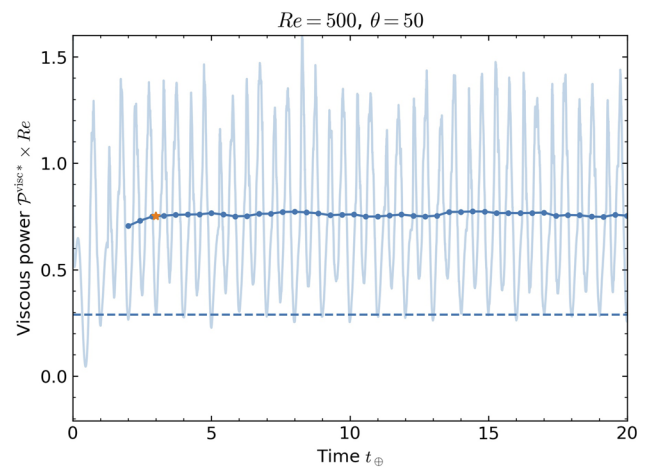


**FIG. 5.** Viscous power per unit area  $\mathcal{P}^{\text{visc}}$  (light blue curve) for the cases  $\theta = 50^\circ$  with longer simulation time. Blue dot: time-averaged value over four oscillation periods. Orange dot: value obtained in the default range  $1 \leq t_{\oplus} \leq 5$ . The default range is sufficient to obtain a steady value. The dashed line shows the laminar solution obtained in [Appendix B](#).

dissipation directly from our model, the reason to use  $\mathcal{P}^{\text{visc}}$  is two-fold: (1) it is consistent with the conventional torque approach to compute the dissipation, and (2) we want to apply the turbulence model that is associated with the surface shear stress (i.e.,  $u_*$ ). A figure showing the time evolution of the three quantities ( $\dot{E}_{\text{int}}$ ,  $\dot{E}_{\text{kin}}$ , and  $\mathcal{P}^{\text{visc}}$ ) for the case at  $Re = 500$  and  $\theta = 0$  is given in the supplementary material (see Fig. S3), verifying the energy balance equation [Eq. (5)]. In [Fig. 4](#), a longer transient period is observed at  $\theta = 50^\circ$ , but the flow eventually reaches a steady state. At  $\theta = 60^\circ$ , we see that  $E_{\text{kin}}$  increases without reaching saturation within the default simulation time  $t_{\oplus} = 5$ . This phenomenon is directly related to the well-known anomalous behavior of the Ekman boundary layer thickness at the so-called *critical latitude*, which in our case is precisely at  $\theta = 60^\circ$  [see, e.g., Sec. 8.07.1.4 in the study by [Tilgner \(2015\)](#)].

[Figures 5 and 6](#) show the viscous power per unit area  $\mathcal{P}^{\text{visc}}$  for the cases  $\theta = 50^\circ$  and  $60^\circ$  with longer simulation time. The time-averaged value over four oscillation periods is plotted in dots. The orange dot indicates the value obtained in the default range,

$1 \leq t_{\oplus} \leq 5$ . As can be seen, for  $\theta = 50^\circ$ , the power reaches a steady value within  $t_{\oplus} \leq 5$ , suggesting that  $t_{\oplus} = 5$  is sufficient for most cases. On the other hand,  $\theta = 60^\circ$  requires a longer transient before reaching a steady value, which approximates the laminar solution. This finding suggests that we should replace the value obtained in the default range by its laminar solution when computing the total dissipation.

### B. Mean velocity profiles

[Figure 7](#) shows the horizontal velocity  $Q^+ = \sqrt{u_x'^2 + u_y'^2} / u_*$  at different Reynolds numbers with  $\theta = 0$  and  $t_{\oplus} = 5$ . The overbar indicates the spatial average on the horizontal plane, and the prime symbol denotes the difference with respect to the boundary velocity, i.e.,  $u_i' = u_i - u_i(z=0)$ . We adopt this notation in order to compare our results to the law of wall formalism [see the study by [Tennekes et al. \(1972\)](#)]. According to the formalism, the velocity profile is divided into three parts: a viscous sublayer  $Q^+ = |z^+$ , a

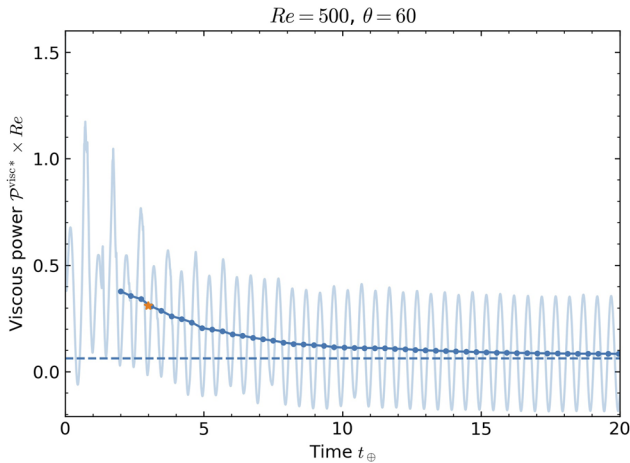


**FIG. 6.** Same as Fig. 5 but for  $\theta = 60^\circ$ . The simulation runs longer than the default range required for the viscous power to reach a steady value, which seems to approach the laminar solution.

buffer layer, and an inertial sublayer  $Q^+ = (1/0.41) \log|z^+| + 5$ . The inertial sublayer is also known as the logarithmic region. As shown in Fig. 7, the velocity profiles approach the one predicted by the law of the wall when  $Re \geq 300$ . A constant slope reveals the presence of a logarithmic region. The inset of Fig. 7 shows the Kármán measure  $\Xi = (|z^+|dQ^+/d|z^+|)^{-1}$  (i.e., the reciprocal of the slope) for  $Re \geq 300$ . A clear logarithmic region develops after  $Re \approx 300$ . In the supplementary material, we show the velocity profiles at different time instants for the case  $Re = 300$  and find that the appearance of a logarithmic layer coincides with an appreciable deviation of the dissipation from its laminar value, as expected from the presence of

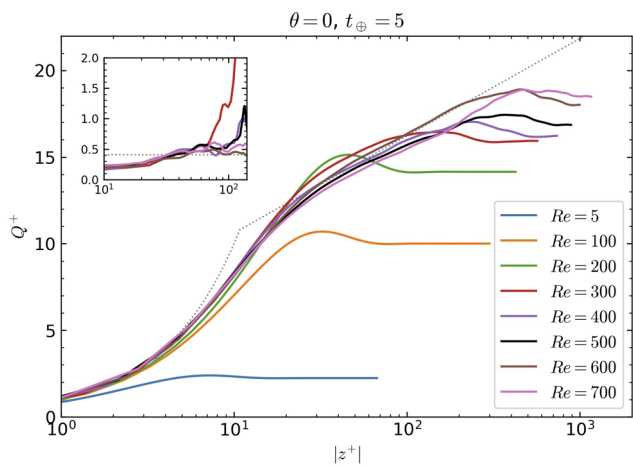


**FIG. 7.** Mean horizontal velocity  $Q^+ = \sqrt{u_x'^2 + u_y'^2}/u_*$  at different Reynolds numbers with  $\theta = 0$  and  $t_\oplus = 5$ . Dotted line:  $Q^+ = |z^+|$  for  $|z^+| \leq 10$  and  $Q^+ = (1/0.41) \log|z^+| + 5$  for  $|z^+| > 10$ . (Inset) Kármán measure  $\Xi = (|z^+|dQ^+/d|z^+|)^{-1}$  for  $Re \geq 300$ . Dashed line:  $\Xi = 0.41$ . The x-axis is  $|z^+|$ , and the y-axis is  $\Xi$ .

turbulence. Besides, the velocity profiles show a maximum above the logarithmic region, which is usually referred to as a *low-level jet* and is also observed for a steady Ekman layer (Deusebio et al., 2014). The fact that the maximum is not well represented in the case of  $Re = 700$  implies that the domain height should be increased accordingly if we want to extend the  $Re$  range.

**C. Similarity theory**

The similarity theory (Csanady, 1967; Spalart, 1989) establishes a relationship between  $u_*$  and  $Re$  of the following form:

$$\frac{U}{u_*} \cos \vartheta + \frac{2}{0.41} \ln \frac{U}{u_*} = \frac{2}{0.41} \ln Re - \frac{1}{0.41} \ln 2 + B, \quad (8)$$

$$\sin \vartheta = \frac{A}{U/u_*}, \quad (9)$$

$$\vartheta = \beta + \frac{2C_5}{Re^2} \left( \frac{U}{u_*} \right)^2, \quad (10)$$

where 0.41 is known as the von Kármán constant. The constants  $A$ ,  $B$ , and  $C_5$  are to be determined by fitting with either experimental or numerical results. We use our numerical solution from  $Re = 300, 400, 500, 600$ , and  $700$  to find the best fit parameters  $A = 5.74$  and  $B = 1.55$  with  $C_5 = -25$  (solid lines in Figs. 8 and 9). The parameters are obtained by performing a least-squares fit. Dashed lines show analytical solutions derived in the laminar regime for comparison. The fitting is good for the friction velocity  $u_*$  but rather inaccurate at  $Re \approx 200$  for the veering angle  $\beta$ . For comparison, results for a steady Ekman layer are plotted in gray:  $u_*$  is about 8% larger while  $\beta$  seems to reach an asymptotic limit at  $Re \geq 10^3$ . Comparison to the model proposed by Sous et al. (2013) is shown

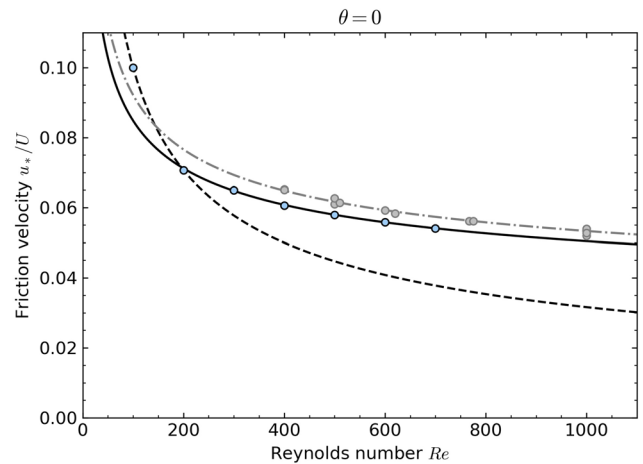


**FIG. 8.** Ratio  $u_*/U$  as a function of the Reynolds number. Blue circles: numerical solution; black line: best fit with  $A = 5.74$ ,  $B = 1.55$ , and  $C_5 = -25$ ; dashed line: laminar solution. Results for a steady Ekman layer from previous studies are plotted with gray circles (Spalart, 1989; Coleman et al., 1990; Coleman, 1999; Shingai and Kawamura, 2004; Marlatt et al., 2012; and Braun et al., 2020); dotted-dashed line is the corresponding best fit with  $A = 5.40$ ,  $B = 0.26$ , and  $C_5 = -52$ . In the turbulent regime,  $u_*$  is about 8% larger than the one for an oscillatory Ekman layer.

06 March 2024 08:08:19



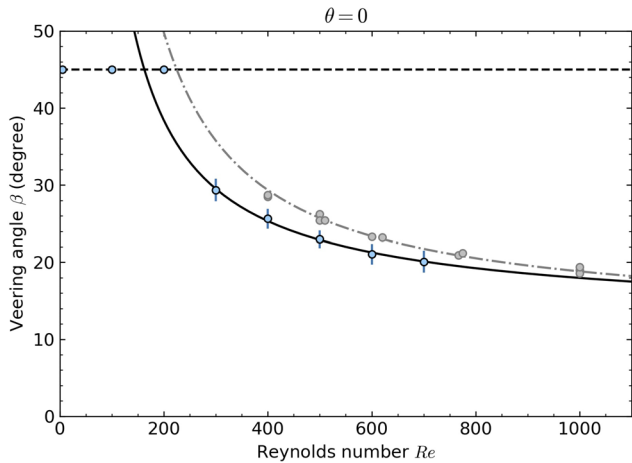


**FIG. 9.** Following Fig. 8. The veering angle  $\beta$  between surface shear stress and boundary velocity seems to reach an asymptotic limit when  $Re \geq 10^3$ .

in the supplementary material (Figs. S5 and S6). Based on our best fit parameters, we compute  $u_*$  and  $\beta$  for a given  $Re$  in the turbulent regime and then use Eq. (7) to obtain the dissipation, comparing it with the one obtained from our local model.

#### D. Viscous dissipation

Figure 10 shows the viscous power per unit area  $\langle \mathcal{P}^{visc*} \rangle$  at each co-latitude  $\theta$ , which we compute by taking a time-average in the default range,  $1 \leq t_{\oplus} \leq 5$ , except for the case  $Re = 300$  (see Sec. IV A). Note that we multiply the power by  $Re$  to remove the viscosity dependence and to see the effect of turbulence. As it can be seen,

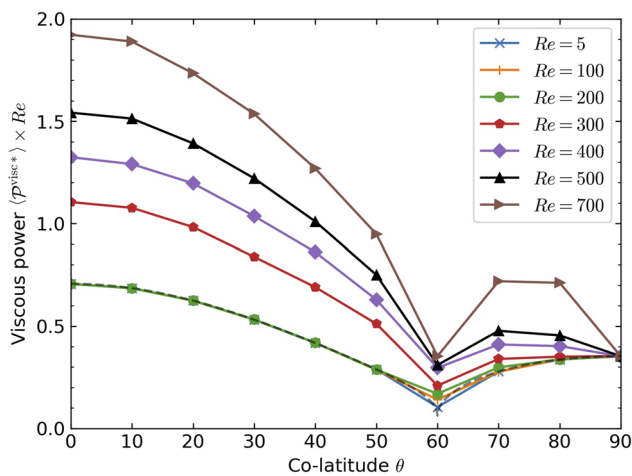


**FIG. 10.** Time-averaged viscous power per unit area  $\langle \mathcal{P}^{visc*} \rangle$  multiplied by  $Re$  at different co-latitudes  $\theta$  ( $^\circ$ ). The gray dash line is computed via  $\mathcal{P}^{visc} = \boldsymbol{\tau} \cdot \mathbf{u}$ , where  $\boldsymbol{\tau}$  and  $\mathbf{u}$  are given by Eqs. (B6)–(B8), (B17), and (B18); the solutions obtained in the laminar regime where the non-linear term is neglected correspond to the cases of small  $Re$ .

when  $Re \geq 300$ , the power increases at almost every  $\theta$  compared to the laminar solution, while the models with  $Re \leq 200$  remain close to the laminar solution. Given  $Re \geq 300$ , the increments are not the same across  $\theta$ . No increment is observed at the equator and is barely present near the critical latitude. As shown in Sec. IV A, the small increment at the critical latitude is the consequence of insufficient simulation time; the power will eventually reach the laminar solution, given long enough simulation time. This latitude variation can be attributed to the orientation of the rotation vector of the fluid, which goes from perpendicular to the flow at the pole to parallel at the equator. When parallel, there is no Coriolis force, and the Ekman boundary layer flow will reduce to the well-studied Stokes type, whose critical Reynolds number for the fully turbulent regime  $Re = 2500$  [see, e.g., the study by Ozdemir *et al.* (2014)] is higher than the present setting.

Figure 11 shows the total global dissipation  $\mathcal{D}_v$  in the boundary layer at different values of  $Re$ . We obtain a global value by integrating the contributions from each numerical simulation at different values of  $\theta$ , using the trapezoidal rule. That means the dissipation in the interval, say, for example,  $10^\circ < \theta < 20^\circ$ , is obtained by linear interpolation. Since the flow is symmetrical along the azimuthal direction and with respect to the equator, we only need to integrate over the range  $0 \leq \theta \leq 90^\circ$ . As we have seen in Sec. IV A,  $E_{kin}$  remains steady for most cases, and the viscous power from surface shear stress will be equal but with an opposite sign to the internal dissipation. Concerning the diverging case at the critical latitude, we replace the value by its laminar solution to avoid overestimation. Therefore, we integrate  $-\mathcal{P}^{visc}$  over the spherical surface to obtain  $\mathcal{D}_v$ . To see the effect of turbulence, we normalize the numerical solution with the laminar solution [Eq. (6)], so it should be very close to unity in the laminar regime if our numerical approach is valid. As can be seen at  $Re = 5$ , the difference in the laminar solution is about  $-4\%$ , which is associated with the limited number of co-latitudes used. The dissipation deviates from the laminar solution when  $Re \geq 300$ . A similar behavior was also observed in the global model by Cébron *et al.* (2019), where dissipation is found to be mainly confined to the

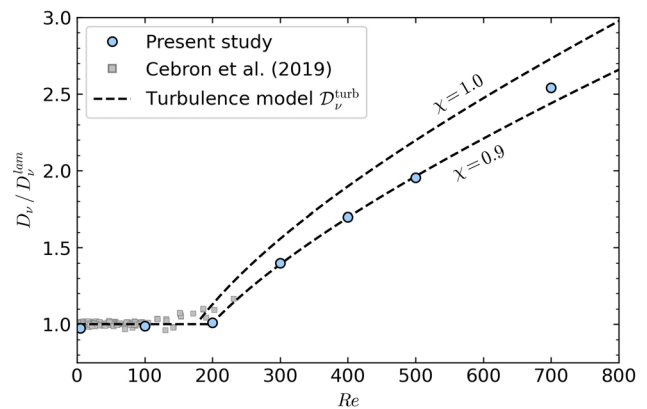


**FIG. 11.** Boundary layer dissipation  $\mathcal{D}_v$  as a function of  $Re$ . The dissipation is normalized by its laminar solution  $\mathcal{D}_v^{lam}$ . Blue circle: present study; gray square: Cébron *et al.* (2019). Dashed line: turbulence model  $\mathcal{D}_v^{turb}$  with  $\chi = 1.0$  and  $\chi = 0.85$ .

boundary layer. Next, we plot the dissipation predicted by the turbulence model  $\mathcal{D}_v^{\text{turb}}$  [Eq. (7)] using a dashed line (Fig. 11). It can be seen that the prediction overestimates the dissipation when  $Re \geq 300$ . Since the turbulence model assumes that the parameter  $k$  at different values of  $\theta$  is the same as the one at the pole, this overestimate is possibly due to the latitudinal dependence shown in Fig. 10. Even from the limited  $Re$  range given in this study, latitudinal variation in the turbulence effect is evident, thus raising the concern of the reliability of the turbulence model based on  $k$ , which is typically treated as a constant in the literature. To accommodate the discrepancy, we introduce a new parameter  $\chi$  and rewrite the turbulent dissipation as

$$\mathcal{D}_v^{\text{turb}} = -2.62\sqrt{2}\chi k I \Delta \Omega^3. \quad (11)$$

We find that  $\chi = 0.85$  marks the lower bound for the results obtained in this study. The dissipation obtained at  $Re = 300, 400,$  and  $500$  falls on the curve of  $\chi = 0.85$ , which means the total dissipation is reduced by about 15% due to the possible laminar flow near the equator. The excess dissipation at  $Re = 700$  shows a hint of increasing dissipation when  $Re$  is even larger.

## V. DISCUSSION AND CONCLUSIONS

We have derived the governing equation for the boundary layer generated by the precession-driven flow in a spherical cavity using a local Cartesian coordinate system. Both the order of magnitude estimation and the numerical solution suggest that the Poincaré term is negligible in the boundary layer if precession is weak. In order to solve the governing equation numerically, we constructed a local Cartesian box model to simulate the boundary layer flow. In the laminar regime, we found that the total energy dissipation, which is computed from the local contributions obtained from the individual box models, is consistent with the laminar value from previous studies based on a global model [e.g., Cébron *et al.* (2019)]. In the turbulent regime, we have found that (1) the flow at certain latitudes (i.e.,  $\theta = 60^\circ$  and  $90^\circ$ ) may remain laminar and (2) the total energy dissipation deviates appreciably from the laminar value. For the flow at the pole,  $\theta = 0$ , the energy dissipation begins to deviate from the analytical laminar expectation when  $Re \geq 300$ , and the flow exhibits turbulent characteristics, such as a logarithmic layer region, allowing us to use an asymptotic similarity formalism. Using this, we have computed the asymptotic curves for both  $u_*$  and  $\beta$  as a function of  $Re$ , which can be used to compute the total energy dissipation in the turbulent regime via turbulence models.

In the conventional turbulence model, the total turbulent dissipation is given as  $-(45\pi/32)kI\Delta\Omega^3$ , where parameter  $k$  is supposed to quantify the asymptotic behavior of the local dissipation in the turbulent regime at high  $Re$ . Note that the derivation of the model implicitly assumes that  $k$  is independent of latitude. Following the same approach as that followed by Cébron *et al.* (2019) to estimate  $k$  via  $k = (u_*/U)^2 \cos \beta$ , we have found that both  $(u_*/U)$  and  $\beta$  at high  $Re$  can be computed from the best fit asymptotic curve obtained at  $\theta = 0$ . In order to recover the laminar solution [Eq. (6)] when  $Re$  goes into the laminar regime, we propose a turbulence model by writing the total dissipation as Eq. (7). The overestimation of the turbulence model, compared to the value obtained from the numerical solution, suggests that the assumption on  $k$  may be inappropriate. At

least for the case of  $Re = 500$ , our numerical solution shows that the flow is not even turbulent at certain latitudes. A thorough investigation on the latitudinal variation on  $k$  combined with an investigation of the flow asymptotic behavior at each latitude would be helpful to establish a more reliable turbulence model. That aside, the uncertainty of the turbulence model given by Eq. (7) is about 15% in the  $Re \leq 700$  range.

The previous study by Deusebio *et al.* (2014) shows that the asymptotic theory applied to the intermediate  $Re$  range ( $400 < Re < 775$ ), where a logarithmic layer is observed, is sufficient to get a good prediction of  $u_*$  and  $\beta$  at high  $Re$  ( $=1600$ ). We adopt the theory for an oscillatory Ekman layer at  $\theta = 0$  not only because we see the logarithmic layer in the flow (Sec. IV B) but also because the theory should be generally unaffected by imposing a time varying boundary velocity. The theory developed by Csanady (1967) and Spalart (1989) is based on the assumption that there exists an overlapping region where the velocity profiles in both the inner layer (viscous sublayer) and the outer layer (free-stream region) match, a fact unaffected by imposing time dependence.

Application to the earth's core is possible since the numerical results presented here are based on the reduced form of the governing equation [Eq. (4)], which is identical to the one derived for a spheroidal cavity such as Earth by Buffett (2021). We are able to reach the earth's parameter regime with the local Cartesian box model, so we do not need to rely on any turbulence model, which will be discussed in the following. Our numerical result shows that the total energy dissipation in the turbulent regime at  $Re = 500$  is 1.86 times of the laminar value. If the damping of FCN shares the same increasing factor, then the effective viscosity will increase by a factor of 3.5, which is still far below the required amount (6 orders of magnitude higher) inferred from the observation. It implies that the electromagnetic coupling may play a significant role in closing the gap.

An accurate calculation of the energy dissipation at the CMB in the moon is unfeasible since we not only lack a proper turbulence model but also because interior models obtained from seismic and gravity measurements are poorly constrained. There are three relevant parameters: (1) the angle between the rotation axes of the core and the mantle, (2) the lunar core radius, and (3) the moment of inertia of the fluid core. There is no direct measurement for the orientation of the core rotation axis. According to the dynamic argument that the lunar CMB flattening is smaller than its Poincaré number, the core is unlikely to share the precession of the mantle (Goldreich, 1967); the core rotation axis should thus be closely aligned with the ecliptic normal. We use the reduced model by Cébron *et al.* (2019) to compute the orientation of  $\Omega_f$  (see Table 1). The plausible range of the core radius obtained from gravity measurements is 200–380 km (Williams *et al.*, 2014; Viswanathan *et al.*, 2019). If we take the core radius as 380 km, then the relative velocity at CMB will be around  $2.72 \times 10^{-2} \text{ m s}^{-1}$ , and the Reynolds number will be  $1.67 \times 10^4$ . We obtain the moment of inertia of the fluid core by taking the moment ratio  $C_f/C = 7 \times 10^{-4}$  (Williams *et al.*, 2014). With our best fit parameters ( $A, B, C_5$ ) and the reduced turbulence model [Eq. (11)], we obtain  $D_v^{\text{turb}} = 72$  or 84 MW for  $\chi = 0.85$  or 1.0, respectively. For a smaller core, say  $Re = 200$  km, with the same moment ratio, the Reynolds number reduces to  $8.79 \times 10^3$  while the dissipation increases by about 10%. For comparison, we also compute the dissipation with the

parameters ( $A = 7.32, B = -2.67$ ) (Sous *et al.*, 2013, the conversion to the present notation is presented in Appendix C) and the conventional turbulence model,  $-(45\pi/32)kI\Delta\Omega^3$  [see Sec. II; e.g., Cébron *et al.* (2019)]; the obtained value is 126 MW, about 60% larger than our result. According to the analysis of lunar laser ranging (LLR) data, the dissipation at CMB is about 58 MW (Williams *et al.*, 2001), 84 MW (Williams *et al.*, 2014), and 73 MW (Williams and Boggs, 2015), respectively. Concerning the uncertainty of the interior model, it is still insufficient to say if our model matches the observation or not, but at least we provide a set of parameters with numerical support, which can be used for the turbulence model. A sensitivity test on the parameters ( $A, B, C_5$ ) shows that (1)  $\beta$  is sensitive to  $A$  and also sensitive to  $C_5$  when  $Re < 10^3$  and (2) the sensitivity of  $u_* / U$  to both  $A$  and  $B$  decreases as  $Re$  increases (see Figs. S7–S9 in the supplementary material).

The implication for planetary cores with turbulent boundary layers should be interpreted with care. In this study, the quoted  $Re$  for Earth and the Moon is obtained based on the laminar solution [e.g., Busse (1968) and Cébron *et al.* (2019)], where the boundary layer is treated in the laminar regime, even though the obtained  $Re$  suggests the other way around. For Earth, the conclusion that the turbulence effect is unlikely to account for the observed FCN damping remains as Earth is at the margin of turbulence. For the Moon, our purpose is to demonstrate a way to forward-compute the dissipation, and a more comprehensive model is needed for future exploration.

We aim to demonstrate that through appropriate formulation, it is feasible to complement the results from global models. By narrowing our focus to the boundary layer exclusively, we can expand the parameter range and explore the turbulent regime. Potential applications of this approach include spin-up, libration, and precessing cylinders (Pizzi *et al.*, 2021).

**SUPPLEMENTARY MATERIAL**

See the supplementary material for the figures of friction velocity showing the comparison between the solutions obtained from Eqs. (2) and (4), velocity profiles for the domain height test, energy balance for the case of  $Re = 500$  and  $\theta = 0$ , velocity profiles of  $Re = 300$  and  $\theta = 0$  at different time instants,  $u_*$  and  $\beta$  as a function of  $Re$  with the comparison to the result of Sous *et al.* (2013), and sensitivity test on ( $A, B, C_5$ ),  $\beta$  as a function of  $\theta$ .

**ACKNOWLEDGMENTS**

We are grateful for the comments and suggestions by all the anonymous reviewers. S.-A.S. would like to thank Benjamin Favier and Philipp Schlatter for the helpful discussion on the numerical methods. The numerical solutions are obtained using NEK5000 Version 20.0-dev at Argonne National Laboratory, Illinois. (available at <https://nek5000.mcs.anl.gov>). S.-A.S. is a Research Fellow of the F.R.S.-FNRS. V.D., J.R., and S.A.T. acknowledge the funding from the European Research Council (ERC) under the European Union’s Horizon 2020 Research and Innovation Program (GRACEFUL Synergy Grant Agreement No. 855677).

**AUTHOR DECLARATIONS**

**Conflict of Interest**

The authors have no conflicts to disclose.

**Author Contributions**

**Sheng-An Shih (施勝安)**: Conceptualization (equal); Data curation (lead); Formal analysis (lead); Methodology (lead); Validation (lead); Visualization (lead); Writing – original draft (lead); Writing – review & editing (equal). **Santiago Andrés Triana**: Conceptualization (equal); Methodology (supporting); Supervision (equal); Writing – review & editing (equal). **Jérémy Requier**: Conceptualization (equal); Writing – review & editing (equal). **Véronique Dehant**: Conceptualization (equal); Funding acquisition (equal); Supervision (equal); Writing – review & editing (equal).

**DATA AVAILABILITY**

The data that support the findings of this study are available from the corresponding author upon reasonable request.

**APPENDIX A: TRANSFORMATION BETWEEN REFERENCE FRAMES AND COORDINATE SYSTEMS**

The solution of  $\Omega_f$  from the study by Cébron *et al.* (2019) is given in the precessing frame where the coordinate system ( $\hat{X}'_p, \hat{Y}'_p, \hat{Z}'_p$ ) is defined such that  $\hat{Z}'_p$  is aligned with  $\Omega_m$  and  $\Omega_p$  is on the  $\hat{X}'_p - \hat{Z}'_p$  plane with the co-latitude  $\alpha$  (Fig. 12). We use  $(\theta_f, \phi_f)$

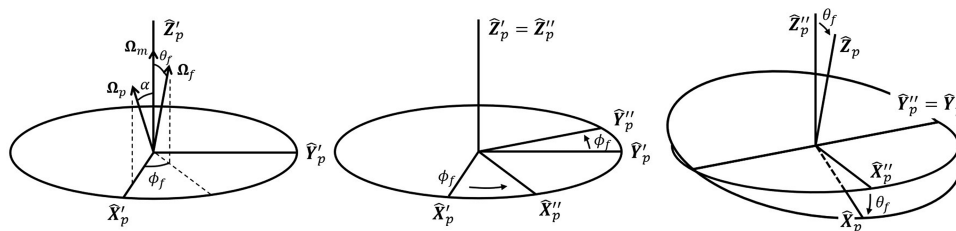


**FIG. 12.** Schematic diagram for the associated vectors and transformations. (Left) The angle between  $\Omega_m$  and  $\Omega_p$  is  $\alpha$ . The co-latitude and longitude of  $\Omega_f$  are  $\theta_f$  and  $\phi_f$ , respectively. Note that the magnitudes and orientations of  $\Omega_m, \Omega_p$ , and  $\Omega_f$  are not to scale. (Middle) Counterclockwise rotation through  $\phi_f$  about  $\hat{Z}'_p$ . (Right) Counterclockwise rotation through  $\theta_f$  about  $\hat{Y}''_p$ .

06 March 2024 08:08:19

to denote the orientation of the fluid rotation vector. Since the global coordinate system  $(\hat{X}, \hat{Y}, \hat{Z})$  defined in the present study has two features— $\hat{Z}$  is aligned with  $\Omega_f$  and it is defined in the fluid frame—we need a series of transformations to adopt the solution in the present study. First, we implement a two-step rotation: (1) rotation about  $\hat{Z}'_p$  in the counterclockwise direction by  $\phi_f$  and (2) rotation about the intermediate axis  $\hat{Y}''_p$  in the counterclockwise direction by  $\theta_f$  [see, e.g., the study by Thornton and Marion (2003)]. The transformation matrices are

$$\lambda_1 = \begin{pmatrix} \cos \phi_f & \sin \phi_f & 0 \\ -\sin \phi_f & \cos \phi_f & 0 \\ 0 & 0 & 1 \end{pmatrix} \quad (\text{A1})$$

and

$$\lambda_2 = \begin{pmatrix} \cos \theta_f & 0 & -\sin \theta_f \\ 0 & 1 & 0 \\ \sin \theta_f & 0 & \cos \theta_f \end{pmatrix}. \quad (\text{A2})$$

The coordinate of a vector  $\mathbf{x}$  in the new coordinate system  $(\hat{X}_p, \hat{Y}_p, \hat{Z}_p)$  is given by  $[\mathbf{x}]_p = \lambda_2 \lambda_1 [\mathbf{x}]'_p$ . The rotations are chosen so that  $\Omega_m$  is on the  $\hat{X}_p$ - $\hat{Z}_p$  plane and leaning toward negative  $\hat{X}_p$  with a co-latitude  $\theta_f$ , which gives the boundary conditions consistent with the ones mentioned in the main text. Second, a transformation from the precessing frame to the fluid frame is given by [see, e.g., the study by Noir and Cébron (2013)]

$$\lambda_3 = \begin{pmatrix} \cos \Omega_f t & \sin \Omega_f t & 0 \\ -\sin \Omega_f t & \cos \Omega_f t & 0 \\ 0 & 0 & 1 \end{pmatrix}. \quad (\text{A3})$$

Finally, in order to solve the governing equations in the local coordinate system, one further transformation is needed, which is given by

$$\begin{cases} \hat{X} = \sin \theta \cos \phi \hat{r} + \cos \theta \cos \phi \hat{\theta} - \sin \phi \hat{\phi}, \\ \hat{Y} = \sin \theta \sin \phi \hat{r} + \cos \theta \sin \phi \hat{\theta} + \cos \phi \hat{\phi}, \\ \hat{Z} = \cos \theta \hat{r} - \sin \theta \hat{\theta}, \end{cases} \quad (\text{A4})$$

where  $\hat{r} = \hat{z}$ ,  $\hat{\theta} = -\hat{y}$ , and  $\hat{\phi} = \hat{x}$  (see Fig. 1). For example, the coordinates of the fluid rotation vector  $\Omega_f$ , which in the  $(\hat{X}'_p, \hat{Y}'_p, \hat{Z}'_p)$  system is given by  $\Omega_f (\sin \theta_f \cos \phi_f, \sin \theta_f \sin \phi_f, \cos \theta_f)$ , in the local coordinate system  $(\hat{x}, \hat{y}, \hat{z})$  are  $(0, \Omega_f \sin \theta, \Omega_f \cos \theta)$ . The coordinates of  $\Omega_p$  and  $\hat{R} \times (\hat{k}_p \times \hat{k}_f)$  are computed in the same way.

### APPENDIX B: ANALYTICAL SOLUTION

We analytically solve Eq. (4) in its dimensional form together with the continuity equation,

$$\frac{\partial \mathbf{u}}{\partial t} + \mathbf{u} \cdot \nabla \mathbf{u} = -\frac{1}{\rho} \nabla P + \nu \nabla^2 \mathbf{u} - 2\Omega_f \times \mathbf{u}, \quad (\text{B1})$$

$$\nabla \cdot \mathbf{u} = 0, \quad (\text{B2})$$

where  $\Omega_f = \Omega_f \hat{k}_f$  is the fluid rotation vector and  $P$  is the reduced pressure, including the centrifugal force. In the local coordinate system, the vector  $\hat{k}_f$  is given by  $\cos \theta \hat{z} + \sin \theta \hat{y}$ , where  $\theta$  is the co-latitude. Following Eq. (3), the boundary conditions require  $\mathbf{u} = 0$  at  $z = -\infty$ ; at  $z = 0$ , the velocities are  $u_x = U \cos \theta \cos(\Omega_f t + \phi)$ ,  $u_y = -U \sin(\Omega_f t + \phi)$ , and  $u_z = 0$ , where  $U$  is the relative velocity of the mantle and  $\phi$  is the longitude. We have to note that the governing equations generally imply a simple rotating fluid with angular velocity  $\Omega_f$ , and this due to the fact that the Poincare term is neglected in the boundary layer of the precession-driven flow. However, precession enters the formulation through the boundary conditions. Nevertheless, the following formulation, borrowed from the classic Ekman layer analysis, serves not only to demonstrate the flow but also to validate the result against known solutions in the literature.

Analytical solutions are available to validate our numerical results in the laminar regime. Equation (B1) can be solved analytically by making some assumptions. First, we assume that the system is horizontally uniform, so the solution must be independent of  $x$  and  $y$ . From the continuity equation  $\nabla \cdot \mathbf{u} = 0$ , we further have  $\partial u_z / \partial z = 0$ . Given that no vertical motion is allowed on the top boundary, we end up with  $u_z = 0$  everywhere. Equation (B1) then becomes

$$\frac{\partial u_x}{\partial t} - 2\Omega_f \cos \theta u_y = -\frac{1}{\rho} \frac{\partial P}{\partial x} + \nu \frac{\partial^2 u_x}{\partial z^2}, \quad (\text{B3})$$

$$\frac{\partial u_y}{\partial t} + 2\Omega_f \cos \theta u_x = -\frac{1}{\rho} \frac{\partial P}{\partial y} + \nu \frac{\partial^2 u_y}{\partial z^2}, \quad (\text{B4})$$

$$2\Omega_f \sin \theta u_x = -\frac{1}{\rho} \frac{\partial P}{\partial z}. \quad (\text{B5})$$

At infinity, given  $u_x = u_y = 0$ , the horizontal pressure gradient should be zero:  $\partial P / \partial x = \partial P / \partial y = 0$ . Since  $u_x$  is independent of  $x$  and  $y$ , the derivative of Eq. (B5) shows that the horizontal pressure gradient is an invariant of height. That means the horizontal pressure gradients are not involved in the horizontal force balance.

From the boundary conditions, we assume that the solutions for the oscillatory Ekman layer are in the form

$$u_x = \Re \left[ e^{i(\Omega_f t + \phi)} q_x(z) \right], \quad (\text{B6})$$

$$u_y = \Re \left[ e^{i(\Omega_f t + \phi) - \frac{i\pi}{2}} q_y(z) \right], \quad (\text{B7})$$

$$u_z = 0, \quad (\text{B8})$$

where  $q_x(z)$  and  $q_y(z)$  are the functions to be solved. Substituting the solutions into Eqs. (B3)–(B5) and solving for  $q_i(z)$ , we end up with

$$q_{x(z)} = C_1 e^{\sigma_+ z} + C_2 e^{\sigma_- z}, \quad (\text{B9})$$

$$q_y(z) = C_1 e^{\sigma_+ z} - C_2 e^{\sigma_- z}, \tag{B10}$$

where  $C_1 = U(\cos \theta - 1)/2$ ,  $C_2 = U(\cos \theta + 1)/2$ , and  $\sigma_{\pm} = \sqrt{\Omega_f/\nu} \sqrt{(1 \pm 2 \cos \theta)}i$ . Notice that the sign of the term  $(1 \pm 2 \cos \theta)$  changes at  $\theta = 60^\circ$  and  $120^\circ$ , so we cannot simply expand  $\sigma_{\pm}$  at this stage. The above-mentioned expression is easy to implement for numerical computation. To get the physical picture, we expand the solution at the three representative co-latitudes:  $\theta = 0^\circ, 90^\circ$ , and  $60^\circ$ . At the north pole ( $\theta = 0$ ), the solution reads

$$u_x = U e^{\frac{z}{\sqrt{2}L_v}} \cos\left(\Omega_f t + \phi - \frac{z}{\sqrt{2}L_v}\right), \tag{B11}$$

$$u_y = -U e^{\frac{z}{\sqrt{2}L_v}} \sin\left(\Omega_f t + \phi - \frac{z}{\sqrt{2}L_v}\right), \tag{B12}$$

where  $L_v = \sqrt{\nu/\Omega_f}$  is the thickness of the steady Ekman layer. Given  $t_0$  and  $\phi_0$ , the solution shows an Ekman spiral, which decays exponentially to the depth. On top of that, the spiral is rotating in the clockwise direction. At the equator ( $\theta = 90^\circ$ ), the boundary drives the fluid in the direction parallel to the rotation vector: there is no Coriolis force acting on the flow. The type of the boundary flow then reduces to the Stokes boundary layer [see, e.g., the study by Landau and Lifshitz (2013)],

$$u_x = 0, \tag{B13}$$

$$u_y = -U e^{\frac{z}{\sqrt{2}L_v}} \sin\left(\Omega_f t + \phi - \frac{z}{\sqrt{2}L_v}\right). \tag{B14}$$

The depth of penetration is usually defined as  $\sqrt{2\nu/\Omega_f} = \sqrt{2}L_v$ . At critical latitudes where one of  $\sigma_{\pm}$  becomes zero, the velocity profile shows a non-decaying component; here is the case of  $\theta = 60^\circ$ ,

$$u_x = U \left[ \frac{-1}{4} e^{\frac{z}{L_v}} \cos\left(\Omega_f t + \frac{z}{L_v}\right) + \frac{3}{4} \cos \Omega_f t \right], \tag{B15}$$

$$u_y = U \left[ \frac{-1}{4} e^{\frac{z}{L_v}} \sin\left(\Omega_f t + \frac{z}{L_v}\right) - \frac{3}{4} \sin \Omega_f t \right]. \tag{B16}$$

That means the flow will penetrate all the way down into the bulk of the fluid and the boundary layer has infinite thickness, which is against the very first assumption of horizontal uniformity—the vertical gradient in velocity is relatively larger than the horizontal ones in the thin boundary layer. This breakdown in the local approximation, already pointed by Bondi and Lyttleton (1953), was shown numerically to spawn internal shear layers, which has negligible contribution to the total dissipation (Hollerbach and Kerswell, 1995).

The shear stress can be computed directly from the velocity. The viscous stress tensor is given by  $s_{ik} = \mu(\partial_i u_k + \partial_k u_i)$ , where  $\mu$  is the dynamic viscosity (note  $\nu = \mu/\rho$  is the kinematic viscosity) [see, e.g., Eqs. (15.2) and (15.8) in the study by Landau and Lifshitz (2013)]. On the top boundary  $z = 0$ , given the normal vector  $\hat{n} = \hat{z}$ , the surface shear stress exerted on the fluid is  $\tau_i = s_{ij} n_j$ , i.e.,  $\tau_x = \mu \partial_z u_x$  and  $\tau_y = \mu \partial_z u_y$ ,

$$\tau_x = \Re \left[ \mu e^{i(\Omega_f t + \phi)} (\sigma_+ C_1 + \sigma_- C_2) \right], \tag{B17}$$

$$\tau_y = \Re \left[ \mu e^{i(\Omega_f t + \phi) - \frac{\pi}{2}} (\sigma_+ C_1 - \sigma_- C_2) \right], \tag{B18}$$

in the local Cartesian coordinate system. Similarly, we give the solutions at the pole and the equator. At  $\theta = 0$ , we have

$$\tau_x = \frac{\mu U}{\sqrt{2}L_v} (\cos \Omega_f t - \sin \Omega_f t) = \frac{\mu U}{L_v} \cos(\Omega_f t - 45^\circ), \tag{B19}$$

$$\tau_y = \frac{-\mu U}{\sqrt{2}L_v} (\sin \Omega_f t + \cos \Omega_f t) = \frac{-\mu U}{L_v} \sin(\Omega_f t - 45^\circ). \tag{B20}$$

Comparison to the boundary velocity shows that the velocity is leading the stress by  $45^\circ$ . We define the veering angle  $\beta$  as the phase difference between the boundary velocity and the surface shear stress (One can also consider the velocity and the stress vectors in complex form, e.g.,  $\mathbf{u} = u_x + iu_y$ , and define the veering angle  $\beta$  as the argument difference between  $\boldsymbol{\tau}$  and  $\mathbf{u}$ , i.e.,  $\beta = \text{Arg}[\boldsymbol{\tau}] - \text{Arg}[\mathbf{u}]$ . However, the definition is only valid at the poles where the vector components have the same magnitude.). It determines the magnitude of the viscous power from  $\boldsymbol{\tau}$ : smaller  $\beta$  means larger power. At  $\theta = 90^\circ$ , we have

$$\tau_x = 0, \tag{B21}$$

$$\tau_y = \frac{-\mu U}{\sqrt{2}L_v} (\sin \Omega_f t + \cos \Omega_f t) = \frac{-\mu U}{\sqrt{2}L_v} \sin(\Omega_f t + 45^\circ). \tag{B22}$$

Comparison with the boundary velocity at  $\theta = 90^\circ$  shows that the stress is leading the velocity by  $45^\circ$ . We note that the phases derived from the  $x$ - and  $y$ -components evolve in opposite directions when  $\theta$  increases from  $0^\circ$  (see Fig. S10 in the supplementary material). Derived from the  $y$ -component,  $\beta$  increases from  $-45^\circ$  at the north pole to  $+45^\circ$  at the critical latitude and then remains until the equator. The flow shows distinct features in the polar region and equatorial region, with the border being  $\theta = 60^\circ$ .

From this Cartesian model, we compute the viscous torque on a spherical surface  $S$  of radius  $R$  by integrating the local contributions:  $\boldsymbol{\Gamma} = \int \mathbf{R} \times \boldsymbol{\tau} dS$ . In a spherical coordinate system, we have  $\tau_\theta = -\tau_y$  and  $\tau_\phi = \tau_x$ , where  $\tau_x$  and  $\tau_y$  are local stresses given by Eqs. (B17) and (B18). The local torque is  $\mathbf{R} \times \boldsymbol{\tau} = -R\tau_\phi \hat{\theta} + R\tau_\theta \hat{\phi}$ . The total torque is given by integrating over the whole spherical surface. After changing to a global Cartesian coordinate system ( $\hat{X}, \hat{Y}, \hat{Z}$ ), we have the torque exerted on the core,

$$\Gamma_X = \int (-\cos \theta \cos \phi \tau_\phi - \sin \phi \tau_\theta) R^3 \sin \theta d\theta d\phi, \tag{B23}$$

$$\Gamma_Y = \int (-\cos \theta \sin \phi \tau_\phi + \cos \phi \tau_\theta) R^3 \sin \theta d\theta d\phi, \tag{B24}$$

$$\Gamma_Z = \int \sin \theta \tau_\phi R^3 \sin \theta d\theta d\phi. \tag{B25}$$

The integrals can be computed numerically. In the end, we have

$$\boldsymbol{\Gamma} = -I\Delta\Omega \frac{\sqrt{\nu\Omega_f}}{R} \left[ (0.258 \sin \Omega_f t + 2.62 \cos \Omega_f t) \hat{X} + (-2.62 \sin \Omega_f t + 0.258 \cos \Omega_f t) \hat{Y} \right], \tag{B26}$$

where  $I = (8\pi/15)\rho R^5$  is the moment of inertia of the sphere. In the fluid frame, the torque circulates in the clockwise direction. Transformed back to the precessing frame [see Eq. (A3)], the torque becomes  $\Gamma = -I\Delta\Omega \frac{\sqrt{v\Omega_T}}{R} (2.62\hat{X}_p + 0.258\hat{Y}_p)$ . We note that the imposed boundary velocity in our local model implies that the vector of differential rotation is given by  $\Delta\Omega = -\Delta\Omega\hat{X}_p$ . In this case, Eq. (B26) agrees with the ones derived from previous studies [e.g., the studies by Yoder (1981), Williams *et al.* (2001), and Cébron *et al.* (2019)], where the results are based on the solution for the spin-over mode (Greenspan, 1968). In principle, the boundary velocity can be modified to represent other types of flow (e.g., spin-up), and the above-mentioned formulation can be applied to derive the corresponding torque [e.g., the study by Noir and Cébron (2013)].

### APPENDIX C: SIMILARITY THEORY

The basic theory is given by Eqs. (8) and (9) with  $\vartheta = \beta$  [or set  $C_5 = 0$ ; see, e.g., the study by Coleman *et al.* (1990)]. To avoid confusion, we label the constants in the study by Sous *et al.* (2013) as  $\hat{A}$  and  $\hat{B}$ . Comparing to their Eqs. (12) and (13), we find that

$$B = -\frac{\hat{A}}{0.41} - \frac{1}{0.41} \ln\left(\frac{z_0}{v/u_*}\right) \quad (C1)$$

and

$$A = \frac{\hat{B}}{0.41}, \quad (C2)$$

where  $z_0 = 0.11v/u_*$  for the smooth surface case. Their best fit result gives ( $\hat{A} = 3.3, \hat{B} = 3.0$ ), which in our convention is ( $A = 7.32, B = -2.67$ ).

### REFERENCES

- Bondi, H. and Lyttleton, R. A., "On the dynamical theory of the rotation of the Earth. II. The effect of precession on the motion of the liquid core," *Math. Proc. Cambridge Philos. Soc.* **49**, 498–515 (1953).
- Braun, L., Younis, B. A., and Weigand, B., "A turbulence closure study of the flow and thermal fields in the Ekman layer," *Boundary-Layer Meteorol.* **175**, 25–55 (2020).
- Buffett, B. A., "Constraints on magnetic energy and mantle conductivity from the forced nutations of the Earth," *J. Geophys. Res.: Solid Earth* **97**, 19581–19597, <https://doi.org/10.1029/92jb00977> (1992).
- Buffett, B. A., "Conditions for turbulent Ekman layers in precessionally driven flow," *Geophys. J. Int.* **226**, 56–65 (2021).
- Buffett, B. A. and Christensen, U. R., "Magnetic and viscous coupling at the core-mantle boundary: Inferences from observations of the Earth's nutations," *Geophys. J. Int.* **171**, 145–152 (2007).
- Buffett, B., Mathews, P., and Herring, T., "Modeling of nutation and precession: Effects of electromagnetic coupling," *J. Geophys. Res.: Solid Earth* **107**, ETG 5-1-ETG 5-14, <https://doi.org/10.1029/2000jb000056> (2002).
- Busse, F. H., "Steady fluid flow in a precessing spheroidal shell," *J. Fluid Mech.* **33**, 739–751 (1968).
- Caldwell, D. R., Van Atta, C. W., and Helland, K. N., "A laboratory study of the turbulent Ekman layer," *Geophys. Fluid Dyn.* **3**, 125–160 (1972).
- Cébron, D., Laguerre, R., Noir, J., and Schaeffer, N., "Precessing spherical shells: Flows, dissipation, dynamo and the lunar core," *Geophys. J. Int.* **219**, S34–S57 (2019).
- Coleman, G. N., "Similarity statistics from a direct numerical simulation of the neutrally stratified planetary boundary layer," *J. Atmos. Sci.* **56**, 891–900 (1999).
- Coleman, G. N., Ferziger, J. H., and Spalart, P. R., "A numerical study of the turbulent Ekman layer," *J. Fluid Mech.* **213**, 313–348 (1990).
- Csanady, G. T., "On the 'resistance law' of a turbulent Ekman layer," *J. Atmos. Sci.* **24**, 467–471 (1967).
- Deleplace, B. and Cardin, P., "Viscomagnetic torque at the core mantle boundary," *Geophys. J. Int.* **167**, 557–566 (2006).
- Deusebio, E., Brethouwer, G., Schlatter, P., and Lindborg, E., "A numerical study of the unstratified and stratified Ekman layer," *J. Fluid Mech.* **755**, 672–704 (2014).
- Fischer, P. F., Loth, F., Lee, S. E., Lee, S.-W., Smith, D. S., and Bassiouny, H. S., "Simulation of high-Reynolds number vascular flows," *Comput. Methods Appl. Mech. Eng.* **196**, 3049–3060 (2007).
- Goldreich, P., "Precession of the Moon's core," *J. Geophys. Res.* **72**, 3135–3137, <https://doi.org/10.1029/jz072i012p03135> (1967).
- H. P. Greenspan, "The theory of rotating fluids," in Technical Report (Massachusetts Institute of Technology, Department of Mathematics, Cambridge, 1968).
- Gwinn, C. R., Herring, T. A., and Shapiro, I. I., "Geodesy by radio interferometry: Studies of the forced nutations of the Earth: 2. Interpretation," *J. Geophys. Res.: Solid Earth* **91**, 4755–4765, <https://doi.org/10.1029/jb091ib05p04755> (1986).
- Herring, T. A., Gwinn, C. R., and Shapiro, I. I., "Geodesy by radio interferometry: Studies of the forced nutations of the Earth: 1. Data analysis," *J. Geophys. Res.: Solid Earth* **91**, 4745–4754, <https://doi.org/10.1029/jb091ib05p04745> (1986).
- Hollerbach, R. and Kerswell, R. R., "Oscillatory internal shear layers in rotating and precessing flows," *J. Fluid Mech.* **298**, 327–339 (1995).
- Ichikawa, H. and Tsuchiya, T., "Atomic transport property of Fe–O liquid alloys in the Earth's outer core  $P, T$  condition," *Phys. Earth Planet. Inter.* **247**, 27–35 (2015).
- Landau, L. D. and Lifshitz, E. M., *Fluid Mechanics: Landau and Lifshitz: Course of Theoretical Physics* (Elsevier, 2013), Vol. 6.
- Lorenzani, S. and Tilgner, A., "Fluid instabilities in precessing spheroidal cavities," *J. Fluid Mech.* **447**, 111–128 (2001).
- Lums, L. I. and Aldridge, K. D., "On viscosity estimates for the Earth's fluid outer core and core-mantle coupling," *J. Geomagn. Geoelectr.* **43**, 93–110 (1991).
- Malkus, W. V. R., "Precession of the Earth as the Cause of Geomagnetism: Experiments lend support to the proposal that precessional torques drive the Earth's dynamo," *Science* **160**, 259–264 (1968).
- Marlatt, S., Waggy, S., and Biringen, S., "Direct numerical simulation of the turbulent Ekman layer: Evaluation of closure models," *J. Atmos. Sci.* **69**, 1106–1117 (2012).
- Mathews, P. and Guo, J., "Viscoelectromagnetic coupling in precession-nutation theory," *J. Geophys. Res.: Solid Earth* **110**, B02402, <https://doi.org/10.1029/2003jb002915> (2005).
- Mathews, P. M., Herring, T. A., and Buffett, B. A., "Modeling of nutation and precession: New nutation series for nonrigid Earth and insights into the Earth's interior," *J. Geophys. Res.: Solid Earth* **107**, ETG 3-1-ETG 3-26, <https://doi.org/10.1029/2001jb000390> (2002).
- Noir, J. and Cébron, D., "Precession-driven flows in non-axisymmetric ellipsoids," *J. Fluid Mech.* **737**, 412–439 (2013).
- Ozdemir, C. E., Hsu, T.-J., and Balachandrar, S., "Direct numerical simulations of transition and turbulence in smooth-walled Stokes boundary layer," *Phys. Fluids* **26**, 045108 (2014).
- Pizzi, F., Giesecke, A., and Stefani, F., "Ekman boundary layers in a fluid filled precessing cylinder," *AIP Adv.* **11**, 035023 (2021).
- Pozzo, M., Davies, C., Gubbins, D., and Alfe, D., "Transport properties for liquid silicon-oxygen-iron mixtures at Earth's core conditions," *Phys. Rev. B* **87**, 014110 (2013).
- Shingai, K. and Kawamura, H., "A study of turbulence structure and large-scale motion in the Ekman layer through direct numerical simulations," *J. Turbul.* **5**, 013 (2004).
- Sous, D., Sommeria, J., and Boyer, D., "Friction law and turbulent properties in a laboratory Ekman boundary layer," *Phys. Fluids* **25**, 046602 (2013).
- Spalart, P. R., "Theoretical and numerical study of a three-dimensional turbulent boundary layer," *J. Fluid Mech.* **205**, 319–340 (1989).

- Stys, C. and Dumberry, M., "A past lunar dynamo thermally driven by the precession of its inner core," *J. Geophys. Res.: Planets* **125**, e2020JE006396, <https://doi.org/10.1029/2020je006396> (2020).
- Tennekes, H., Lumley, J. L., Lumley, J. L. *et al.*, *A First Course in Turbulence* (MIT Press, 1972).
- Thornton, S. T. and Marion, J. B., *Classical Dynamics of Particles and Systems* (Cengage Learning, 2003).
- Tilgner, A., "Rotational dynamics of the core," *Treatise Geophys.* **8**, 183–212 (2015).
- Triana, S. A., Trinh, A., Requier, J., Zhu, P., and Dehant, V., "The viscous and ohmic damping of the Earth's free core nutation," *J. Geophys. Res.: Solid Earth* **126**, e2020JB021042, <https://doi.org/10.1029/2020JB021042> (2021).
- Viswanathan, V., Rambaux, N., Fienga, A., Laskar, J., and Gastineau, M., "Observational constraint on the radius and oblateness of the lunar core-mantle boundary," *Geophys. Res. Lett.* **46**, 7295–7303, <https://doi.org/10.1029/2019gl082677> (2019).
- Williams, J. G. and Boggs, D. H., "Tides on the Moon: Theory and determination of dissipation," *J. Geophys. Res.: Planets* **120**, 689–724, <https://doi.org/10.1002/2014je004755> (2015).
- Williams, J. G., Boggs, D. H., Yoder, C. F., Ratcliff, J. T., and Dickey, J. O., "Lunar rotational dissipation in solid body and molten core," *J. Geophys. Res.: Planets* **106**, 27933–27968, <https://doi.org/10.1029/2000je001396> (2001).
- Williams, J. G., Konopliv, A. S., Boggs, D. H., Park, R. S., Yuan, D.-N., Lemoine, F. G., Goossens, S., Mazarico, E., Nimmo, F., Weber, R. C. *et al.*, "Lunar interior properties from the grail mission," *J. Geophys. Res.: Planets* **119**, 1546–1578, <https://doi.org/10.1002/2013je004559> (2014).
- Yoder, C. F., "The free librations of a dissipative Moon," *Philos. Trans. R. Soc. London, Ser. A* **303**, 327–338 (1981).
- Zhang, J. and Dumberry, M., "Viscous dissipation in the fluid core of the Moon," *J. Geophys. Res.: Planets* **126**, e2021JE006966, <https://doi.org/10.1029/2021je006966> (2021).